*Tellus (1994), 46A, 465–480*
*Printed in Belgium – all rights reserved*


**TELLUS**
*ISSN 0280–6495*

# ENSO prediction experiments using a simple ocean-atmosphere model

By DENG-HUA WU[1], DAVID L. T. ANDERSON[2] and MICHAEL K. DAVEY[3]*, [1]*Department of Meteorology, University of Maryland, College Park MD 20742 USA*, [2]*Atmospheric, Oceanic and Planetary Physics, University of Oxford, Parks Road, Oxford OX1 3PU, England*, and [3]*Hadley Centre, UK Meteorological Office, London Road, Bracknell RG12 2SY, England*

(Manuscript received 9 August 1993; in final form 14 March 1994)

ABSTRACT

A coupled model consisting of a reduced gravity ocean and an empirical atmosphere is developed to investigate predictability of ENSO. The ocean model has no seasonal cycle, and is forced only by zonal wind stress anomalies. The empirical atmosphere is constructed by using statistical techniques to relate observed wind stress anomalies directly to the sea surface temperature anomalies simulated by the model. The focus of this study is on detailed analysis of individual predictions, as well as on statistical scores from an ensemble of predictions. The model can in general successfully predict an event up to about one year in advance, but the model has little ability to predict low amplitude variability that is not related to ENSO. Predictions based on POP analysis of the ocean model data are also made for several ENSO events, with skill comparable to that of the dynamical coupled model.

## 1. Introduction

The El Niño/Southern Oscillation (ENSO) phenomenon in the tropics is an important example of large scale ocean-atmosphere interaction in climate variability. It can be regarded as an oscillation between El Niño (the warm phase) and La Niña (the cold phase). During El Niño events, anomalously warm sea surface temperatures (SST) are typically observed in the central-eastern Pacific with small negative SST anomalies in the west. The associated atmospheric change is a weakened Walker circulation or shift of the convective centre from the west to central Pacific, and a decrease of sea level pressure difference between Tahiti and Darwin (a measure of the Southern Oscillation). Extensive studies have been made of the mechanisms responsible for the oscillation, mostly by using coupled ocean-atmosphere models with limited but essential physical processes: see McCreary and Anderson (1991) or Neelin et al. (1994) for a review. Recently, several forecasting models have been proposed for the prediction of ENSO, ranging from purely statistical methods through intermediate coupled models to fully coupled GCMs. Such models have been reviewed by Latif et al. (1994): all of the models considered have some skill in predicting ENSO events about 6–12 months in advance, but the dynamically coupled ocean-atmosphere models (Cane et al., 1986, in particular) have longer useful lead times.

The success of these model predictions comes presumably from the quasi-cyclic character of ENSO and could depend strongly on how well the models can reproduce the key spatial and temporal relationships between the wind stress and SST anomalies. In order to reproduce such observed relations without invoking atmospheric dynamics, Latif and Flügel (1991) and Barnett et al. (1993) have developed alternative coupled models that consist of a physically-based dynamical ocean model coupled to an empirical atmosphere. The latter is trained by determining a

* Corresponding author.

statistical relation between the observed wind and observed SST anomalies, which are in turn related to modelled SST anomalies by another regression matrix. Since there are many ways to construct such an empirical atmosphere, it is of interest to try experiments based on different approaches. The prediction model described in this paper differs from previous models in that the atmospheric component is derived by relating observed wind anomalies directly to model SST anomalies produced by those winds; further, the ocean is itself a north–south symmetric anomaly model with no seasonal cycle in the prescribed background state.

The paper is organized as follows. Section 2 contains a description of the ocean model and of the empirical atmosphere, illustrated using data from the ocean model forced by observed winds. A description of principal oscillation pattern (POP) analysis and its application to data from the ocean model to find a dominant ENSO-related mode is given in Section 3. The coupled model prediction experiments are described in Section 4, followed by a comparison in Section 5 with a prediction scheme based on POP analysis. Discussion and a summary of the present study are given in Section 6.

## 2. Coupled model description

### 2.1. The ocean model

The ocean model used in this study consists of a linear reduced gravity model with one active layer, simulating layer depth changes $h$ and associated currents $\boldsymbol{u}$. The long-wave approximation is used, and the model is forced only by zonal wind stress anomalies (i.e., perturbations from monthly mean climatology). The ocean has a rectangular domain, and north–south symmetry is imposed. There is a separate equation for SST anomalies $T$:

$$T_t + (u + \delta u_s)\,\bar{T}_x + w_s \bar{T}_z + w_o(T - T_{sub})/H_o = \nu \nabla^2 T - dT^3. \quad (1)$$

Here $\bar{T}_x$ is a constant zonal SST gradient, $\bar{T}_z$ depends on longitude only (increasing eastward), and background upwelling $w_o$ depends on latitude only (decreasing poleward). The upwelled temperature anomaly $T_{sub}$ depends linearly on $T$ and $h$, with the coefficient of $h$ increasing eastward. The surface velocity anomaly $\boldsymbol{u}_s$ is determined by a linear equilibrium balance of wind stress, Coriolis force and friction, and gives rise to an upwelling anomaly $w_s$. No seasonal information is contained in the background state, and the only nonlinear term is the cubic temperature anomaly damping term. This model has previously been used to investigate external impacts on ENSO variability (Wu et al., 1993a), and further details of the model formulation and parameter values can be found there.

### 2.2. The empirical atmosphere

The empirical atmosphere to relate the wind stress anomaly to model SST variations was derived as follows. The ocean model was forced by using the observed monthly Florida State University (FSU) wind stress anomalies (Goldenberg and O'Brien, 1981) from January 1961 through January 1992 to obtain a 31-year record of monthly SST. Only the zonal wind component was used. The wind stress was detrended by the same technique used in Cane et al. (1986) to remove a possible long term trend; namely, the anomaly was calculated relative to the previous four-year mean with seasonal dependence. A drag coefficient of $1.125 \times 10^{-3}$ and air density of $1.2\ \mathrm{Kg\,m^{-3}}$ were used to convert the FSU pseudostress to the stress used to drive the ocean model. There is no seasonal cycle in either the forcing or the mean state in this model.

Having obtained model SST anomalies, a statistical relation between anomalies of the simulated SST and the observed wind stress used as the driving force for the simulation was obtained. The method is the same as that used in companion papers by Balmaseda et al. (1994) and Davey et al. (1994). Simulated monthly SST anomalies $T^{sim}_{mn}$, with index $m$ standing for space ($M$ points) and $n$ for time ($N$ months), can be expressed by singular value decomposition as:

$$T^{sim}_{mn} = \sum_{k=1}^{N} E_{mk} \lambda_k C_{nk}, \quad (2)$$

where the $E_{mk}$ are normalised components of the $k$th empirical orthogonal function (EOF), $\lambda_k$ contains variance information, and $C_{nk}$ is the normalised coefficient of EOF $k$ at time $n$. At any

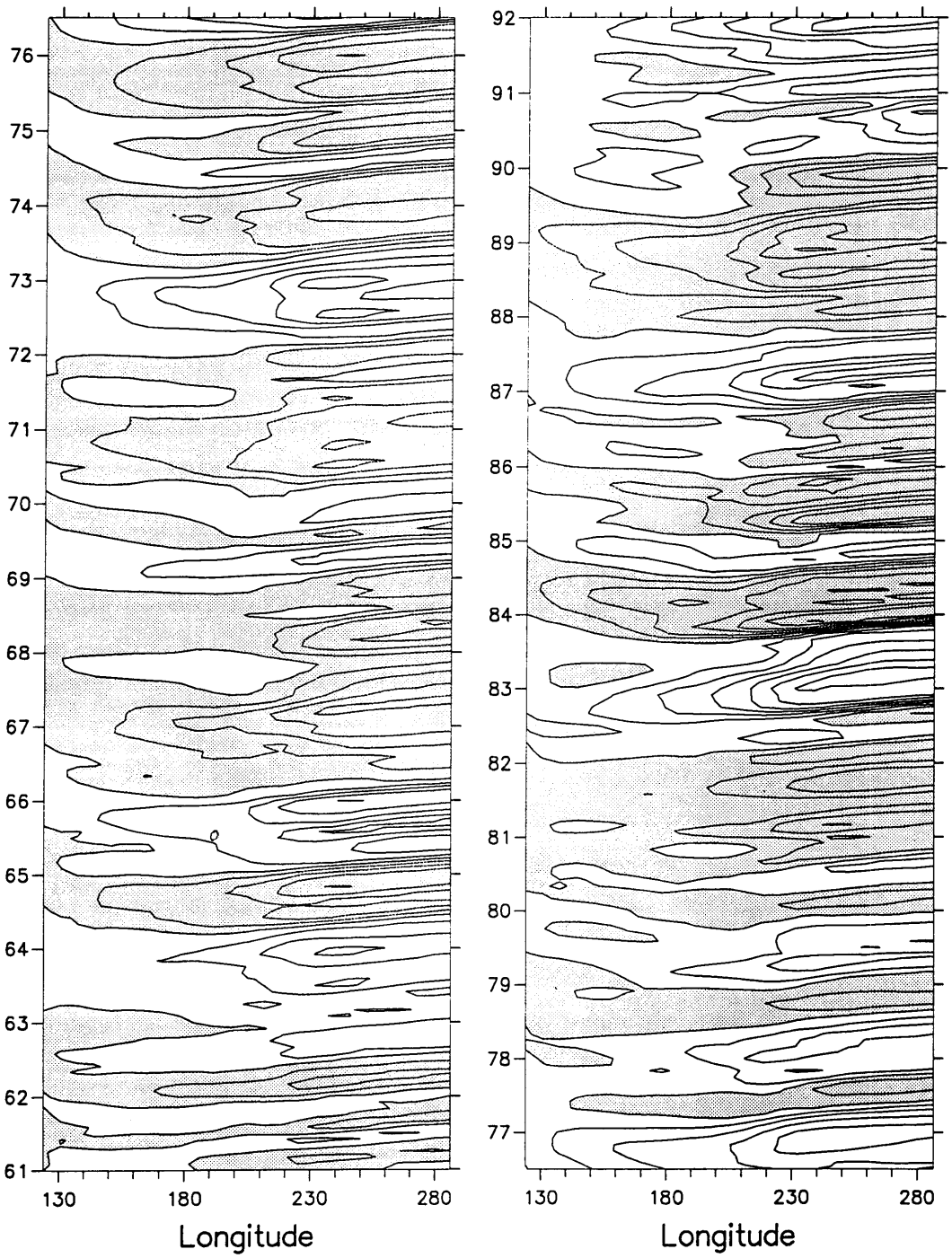


*Fig. 1.* Model sea surface temperature anomalies along the equator, from the simulation forced by detrended FSU wind stress anomalies for 1965 to 1992. Contour interval 0.5°C, negative values shaded. Labels indicate the beginning of the respective years.

time an SST anomaly pattern $T$ can be projected onto the EOFs to obtain coefficients

$$A_k = \sum_{m=1}^{M} E_{mk} T_m. \tag{3}$$

We use $L$ (typically 3) of these coefficients as predictors of wind stress anomalies $\tau$, to obtain

$$\tau_m = \sum_{l=1}^{L} W_{ml} A_l, \tag{4}$$

where the $W_{ml}$ are components of the $l$th associated wind stress pattern. The associated wind stresses are obtained from the observed stress $\tau^{obs}$ used in the simulation:

$$W_{ml} = \sum_{n=1}^{N} \tau_{mn}^{obs} C_{nl}/\lambda_l. \tag{5}$$

This formula gives a least squares fit of reconstructed to observed wind stress anomalies.

The $T^{sim}$ values actually used for the decomposition (2) started from January 1965, since the wind anomaly was calculated relative to the previous 4-year mean. The first few leading EOFs (arranged according to decreasing eigenvalues $\lambda_k$) explain a large fraction of the total variance of $T^{sim}$ in the model.

Fig. 1 shows the time evolution of SST anomalies along the equator, calculated by using the observed wind. It can be seen that the model captures every warm/cold event during the period shown, with the amplitudes mainly confined to the central-eastern Pacific. However, the spatial structure (not shown) of the anomalies is too concentrated in the equatorial region compared with that observed. Similar time series of depth anomalies $h$ (not shown) reveal prominent westward propagation 5° off the equator, and faster eastward propagation along the equator. In contrast to $T$, there is considerable $h$ activity in the west Pacific (particularly off the equator) as well as in the central-east Pacific. The equatorial $h$ propagation from the west to east Pacific is slower than the rapid eastward $T$ movement in the east Pacific seen in Fig. 1.

It is useful to examine the extent to which the empirical atmosphere can reflect the actual physics of the coupling between the ocean and atmosphere. The first EOF pattern of $T^{sim}$, which accounts for 87.3% of the $T$ variance in the forced run, is shown in Fig. 2a, with the associated wind pattern in Fig. 2b. The peaks of the timeseries of coefficients for the first EOF correspond well with ENSO events in the simulation. The amplitude of this EOF pattern is largest (warm as shown) in the central-eastern Pacific, and is very similar to the SST anomaly patterns found during ENSO events as simulated in the model. The associated zonal wind pattern has largest amplitude (westerly as shown) over the west Pacific, with a maximum centered near the dateline. The meridional scale of the wind is much larger than that of SST. These are all characteristics also found in observations (Rasmusson and Carpenter, 1982; Latif et al., 1992). The distributions of the SST and wind patterns are such that a westerly wind anomaly in the central-western Pacific is associated with a warm SST anomaly in the central-eastern Pacific. There is no significant easterly wind associated with the EOF 1 SST anomaly, in contrast to the response of a Gill-type (Gill, 1980) atmospheric model to such a pattern. The second and third SST EOFs explain

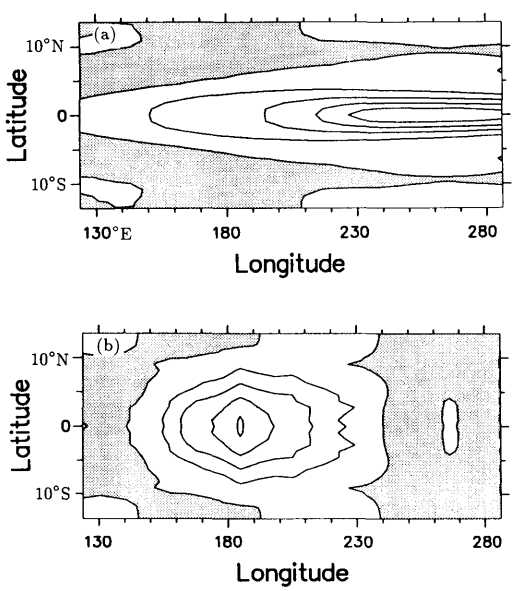


*Fig. 2.* (a) The first EOF pattern of simulated SST anomalies. (b) The associated zonal wind stress anomalies. Contour intervals are arbitrary, negative values are shaded.

much less variance (8.4% and 2.0%) than does the first EOF. Their associated wind patterns also have wind anomalies that tend to be located over and west of temperature anomalies of the same sign.

## 3. POP analysis and the mechanism for interannual variability

The model ocean has previously been coupled to a simple Gill-type dynamical atmosphere, as described in Wu et al. (1993a). By investigating wave components, it was suggested there that the delayed oscillator mechanism played a major role in generating the interannual variability in that model. Here we take an alternative approach, and use POP analysis (Hasselmann, 1988; Von Storch et al., 1993) to examine the mechanism operative in the ocean model forced by observed winds. By applying POP analysis, data can be re-expressed as a superposition of POP spatial patterns and timeseries, where the POP patterns represent independent modes that would evolve as decaying oscillations in the absence of forcing. An oscillating mode has "real" and "imaginary" spatial patterns $pop_R$ and $pop_I$, and characteristic period $\tau$ and $e$-folding decay time $D$. (See Appendix for details.)

If the system is dominated by one particular POP mode, then insights into the mechanism operating in the system can be obtained by examining the spatial patterns and time behaviour. To do so, measures are needed to pick out useful or significant POP modes. One is the matching of the oscillation period $\tau$ to the interannual ENSO timescale. Another is how well the actual POP mode evolution resembles the oscillation of an unforced POP mode: this is examined by taking lag correlations between timeseries for $pop_R$ and $pop_I$. A well-behaved POP mode will have a positive maximum correlation at a lag of $\tau/4$ with the imaginary part leading the real part. In addition, the decay timescale of a POP mode should not be much shorter than its oscillation period, otherwise the POP pattern will virtually disappear before one cycle has completed.

Another indicator is a comparison of the variance accounted for by a particular POP mode with that of other modes. A useful POP mode should account for a significant fraction of the variance of the original data. However, since the POP modes are not orthogonal to each other, the variance of each mode is not additive and care is needed in interpreting this. A further indicator is correlation of the POP coefficients with a given timeseries such as the timeseries of SST anomalies averaged over the Niño3 region (150°W–90°W, 5°S–5°N). A POP mode representing ENSO can be expected to have higher correlation with this timeseries than other (non-ENSO) modes.

Since coherent structures in the atmospheric and oceanic variables are observed during ENSO events, it is useful to examine the oscillatory patterns in these variables as a unified system. Anomalies of sea surface temperature, the upper layer depth and zonal wind stress are used in the following analysis (cf. Latif et al., 1993). The anomalies for different variables were normalized by their respective standard deviations before being combined to form a unified dataset. POP analysis was applied, using the first few EOFs of the combined data and their corresponding timeseries.

For the forced run, 20 EOFs were retained for POP analysis. The fraction of total variance of the combined dataset explained by these EOFs is 91%. Sensitivity experiments showed that the number of EOFs retained in the analysis did not have a significant influence on the POP mode of interest. The spatial structures of the first three EOFs for SST and zonal wind (not shown) are fairly similar to those obtained by applying EOF analysis to the SST anomalies alone and determining the associated winds as in Subsection 2.2. The POP mode which best represents ENSO in the simulation, according to the above criteria, has an oscillation period of 31.5 months and $e$-folding time of 17 months. Lag correlations of the timeseries of real and imaginary POP coefficients for that mode show that a positive maximum correlation of about 0.65 occurs at a lag time of about 8 months with the imaginary coefficient leading the real one. The maximum correlation of the POP coefficients with Niño3 SST anomalies is about $-0.8$ for the imaginary part, indicating that this POP mode is likely to be an ENSO mode. In addition, this POP mode has the largest fraction of variance compared to other POP modes (24.4% of the variance obtained when summing all POP modes, 63.9% of the total variance of the unified dataset: see Appendix). Together, these results

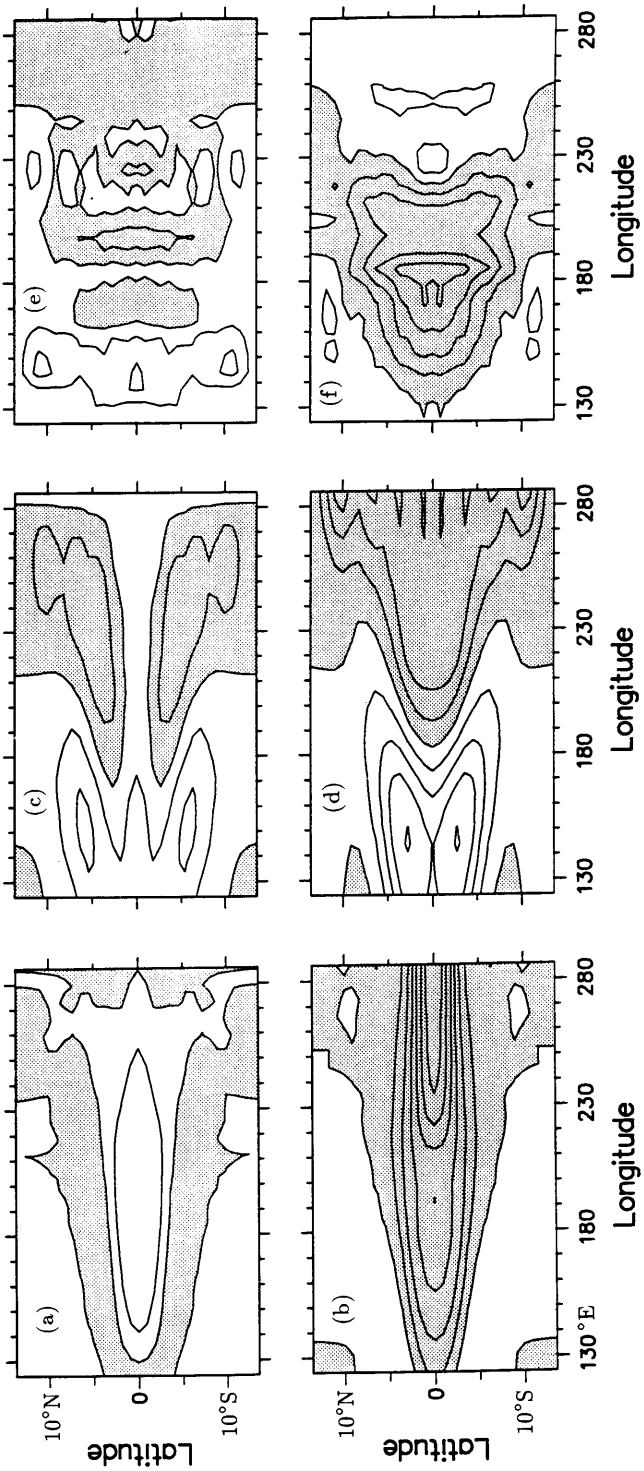


*Fig. 3.* Spatial patterns of anomalies for the dominant ENSO-related POP mode in the simulation run. This POP mode has period 31.5 months and *e*-folding decay time 17 months. Here real patterns $pop_R$ are associated with transition ENSO phase, while imaginary patterns $pop_I$ are associated with peak ENSO phase. (a) real SST, (b) imaginary SST, (c) real depth, (d) imaginary depth, (e) real zonal wind stress, (f) imaginary zonal wind stress. Contour intervals are arbitrary for each physical field, but are the same for the real and imaginary components. Negative values are shaded.

suggest that this POP mode represents the dominant interannual behaviour in the forced simulation fairly well, and that it is related to ENSO, with the imaginary component corresponding to ENSO peaks.

Fig. 3 shows the POP patterns $pop_R$ and $pop_I$, for this ENSO-like mode, with $pop_I$ representing a cold extreme as shown. For a freely evolving POP oscillation the patterns appear in the sequence $pop_R \rightarrow (-pop_I) \rightarrow (-pop_R) \rightarrow pop_I \rightarrow pop_R \cdots$. In the simulation this sequence is followed during main ENSO events, but at other times the POP timeseries are less coherent and have low amplitude. The real temperature pattern $pop_R$ shows a weak anomaly in the central Pacific, while the imaginary pattern $pop_I$ has large amplitude in the central-eastern Pacific. The anomalies in temperature and layer depth are positively correlated, especially in the central-eastern equatorial Pacific: a warm event is associated with a deeper thermocline in the east Pacific, and vice versa. The real pattern represents a transition phase, and the imaginary pattern corresponds to the peak phase of the ENSO cycle. The big difference in the amplitudes of the real and imaginary patterns of SST anomaly (Fig. 3) suggests that the temperature anomaly is basically a standing oscillation, in this POP filtered view, in contrast to the situation in the layer depth anomaly patterns, where the real and imaginary patterns have comparable amplitudes, suggesting propagation (cf. Latif et al., 1993a).

In the peak phase of a cold event, large negative anomalies of the layer depth are observed in the eastern Pacific, with positive off-equatorial maxima in the west Pacific; a quarter of a period later, the negative eastern anomalies are replaced by weak positive anomalies in the equatorial region. This can be attributed to propagation of the positive anomalies accumulated in the western Pacific during the peak cold phase. In the next half cycle, the positive anomalies grow in the central-eastern Pacific and then decay due to the arrival of negative anomalies from the west. During a peak cold (warm) phase, negative (positive) zonal wind anomalies in the central-western Pacific produce negative (positive) layer depth anomalies to the east and positive (negative) anomalies to the west, and the latter may form the seed of negative feedback effects to reverse the peak, as in the delayed oscillator scenario.

## 4. Prediction experiments

Prediction experiments were carried out using the empirical atmosphere, constructed with 3 SST EOFs, coupled to the ocean model. The initial conditions were taken from the run forced with FSU winds, which will be referred to as the control run. Because the atmospheric model is truncated to 3 associated wind patterns immediately after starting a prediction, errors relative to the forced run are effectively introduced into the system immediately. These errors, however, are mostly of small scale; their impact on large scale, interannual variability remains unclear since small scale features in the atmosphere are likely to be filtered out by the ocean. On an interannual timescale the winds reconstructed from the control $T$ using 3 SST EOFs generally fit well the winds used to force the control run, the main difference being an underestimation of the 1982/83 peak wind anomalies.

The predictions were started every 3 months (1 January, 1 April, 1 July and 1 October); and each prediction was performed for two years. The first prediction considered here was started in January 1965, and the last one in October 1989: 100 prediction experiments in total. Before investigating ensemble features of the predictions, individual predictions of some typical ENSO episodes are examined in order to gain some insights into how the model captures or misses a target event. For most results presented, the predictions are compared with the control run.

### *4.1. Case studies*

Latif et al. (1993b) have considered five cases of typical warm and cold events, using four start times for each case. For comparison we considered the same events in detail: the 1972/73 and 1986/87 warm events and the following cold events, and the 1982/83 warm event (see Table 1).

Figs. 4a–e shows the time evolution of SST anomalies in the Niño3 region for the control run and 20 predictions for the 5 cases. The predictions, in general, follow the control run fairly well, except for the 1986/87 warm event in which predictions starting in April and July 1986 diverged from the control run soon after the start. For the 1972/73 warm event, each prediction warmed, but for predictions starting in October 1971 and January

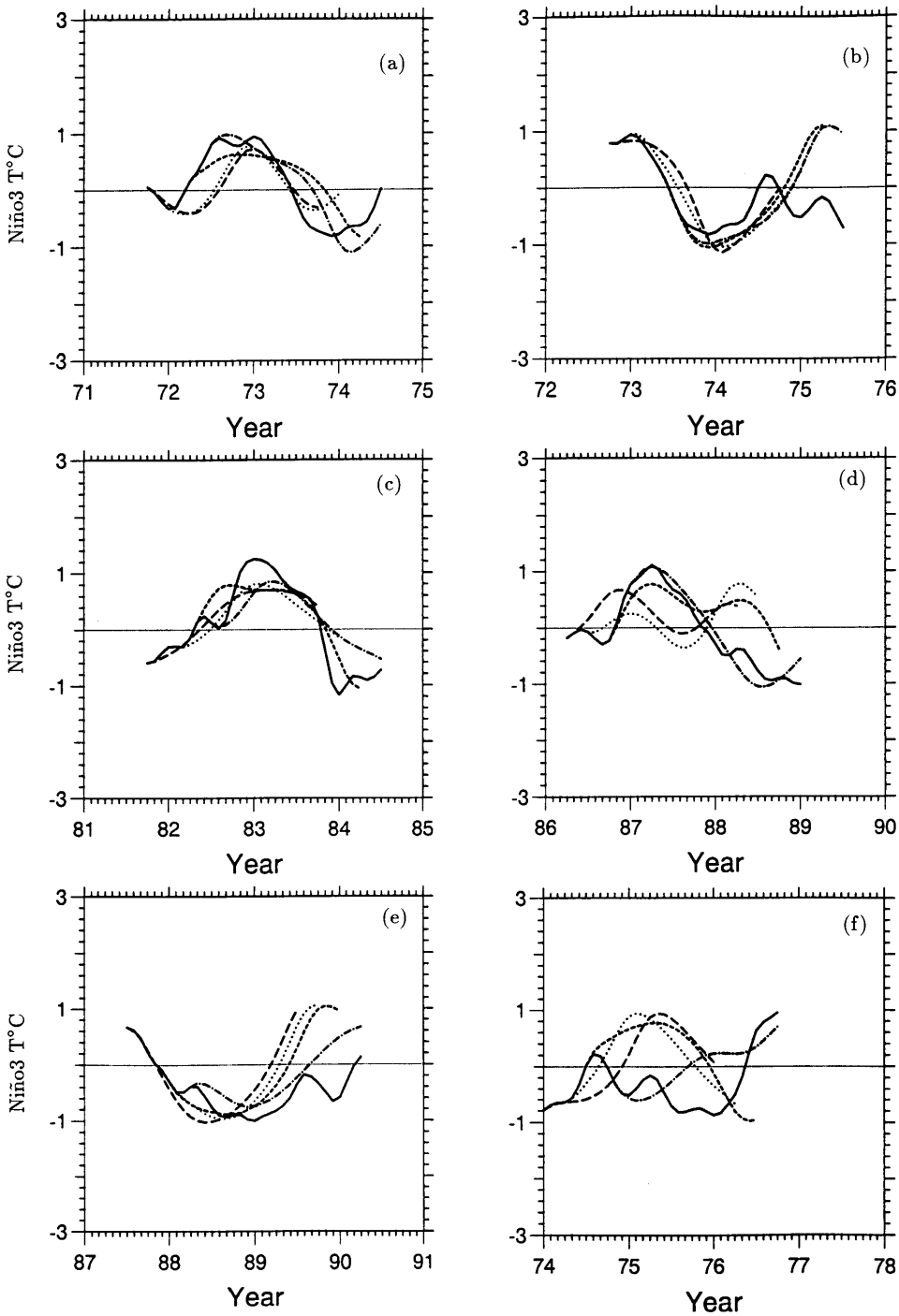


*Fig. 4.* SST anomalies in the Niño3 region for the control run (solid) and predictions using the empirical atmosphere (dashed), for 5 warm and cold ENSO cases and for the 1974/75 non-event (see Table 1 for start dates). Initial conditions for the predictions were taken from the control run.

Table 1. *Starting times of prediction experiments for ENSO case studies*

| (a) 1971/72 warm | (b) 1972/73 cold | (c) 1982/83 warm | (d) 1986/87 warm | (e) 1987/88 cold | (f) 1974/75 non-event |
|---|---|---|---|---|---|
| July 1/71 | Jul./72 | Jul./81 | Jan./86 | Apr./87 | |
| Oct./71* | Oct./72* | Oct./81* | Apr./86* | Jul./87* | Jan./74 |
| Jan./72* | Jan./73* | Jan./82* | Jul./86* | Oct./87* | Apr./74 |
| Apr./72* | Apr./73* | Apr./82* | Oct./86* | Jan./88* | Jul./74 |
| Jul./72* | Jul./73* | Jul./82* | Jan./87* | Apr./88* | Oct./74 |

The 20 experiments marked (*) are shown in Figs. 4a–e and used for the correlations in Fig. 5.

1972 the change from negative to positive anomalies occurred about 4 months late. The correlation $r$ as a function of lead time between these 20 predictions and both the control run and the observed Niño3 anomalies are shown in Fig. 5. Using the control run, the correlation drops rapidly in the first 5 months from $r = 1$ at zero lead, followed by a plateau above 0.8 up to a lead time of about 15 months. The predictions also correlate well with the observations, with $r$ rising from 0.7 at zero lead to a similar 0.8 plateau. These results imply useful predictions more than one year in advance, at least as far as events are concerned. (In the context of ENSO prediction $r > 0.5$ is generally considered useful.)

The 1974/75 "non-event" is shown in Fig. 4f. In the observations, there seemed to be an incipient ENSO in the middle of 1974, but it aborted later in 1974. Many coupled models, however, fail to reproduce this behaviour in hindcast experiments and instead predict a warm event (according to information collected as part of a Tropical Ocean Global Atmosphere Numerical Experimentation Group (TOGA-NEG) hindcast intercomparison). The present model was also unable to follow the control run, and produced a spurious warm event for predictions starting in January, April, and July 1974.

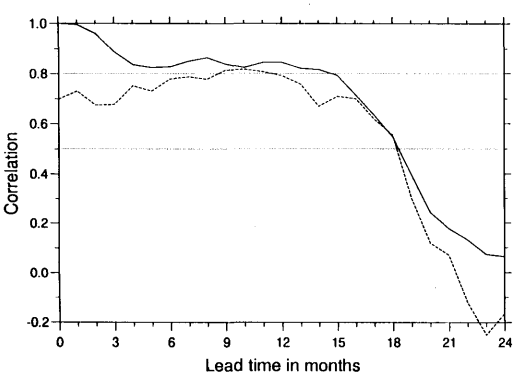


*Fig. 5.* Correlation, as a function of lead time, of predicted SST anomalies in the Niño3 region with control (solid) and observed (dashed) values: 20 predictions for 5 warm and cold ENSO cases were used (see Table 1).

The timing of the 1982/83 case is predicted rather well. Each prediction, starting as early as July 1981 or as late as July 1982, was able to produce a warm event initiated in late 1982 and decaying around the end of 1983. Except for the early peak in the April 1982 prediction, the peaks in each prediction were at approximately the same time. For example, for the prediction starting in July 1981 a warm event was not initiated until late 1982 and the maximum amplitude was around March 1983; while in the prediction starting in July 1982, a warm episode began to develop soon after the start of the prediction and the peak amplitude was seen around April 1983.

The 1986/87 warm event was the least well hindcast. In this case, predictions starting from different initial conditions diverged considerably. For the prediction started in January 1986, a warm event soon developed, which was not seen in the control run until the end of 1986. Predictions starting in April and July 1986 developed oscillations which have little similarity to the control run. The best result for this case is the prediction starting in January 1987, when the warm event was already underway.

To understand why the prediction model behaves so differently from one event to another, we examined more closely how the model evolves from a given initial condition. For this purpose,

the coefficients $A_k$ for the EOF projections and the associated wind anomalies (see eqs. (3) and (4)) were analyzed. The reason for using these coefficients is twofold. First, if a prediction were very accurate, then its $A_k$ would follow closely the timeseries for the control run; the errors would be entirely due to the truncation of EOFs retained in the coupled integration. Therefore evolution of $A_k$ associated with each EOF provides another measure of the model prediction. Moreover, since the largest amount of the variance of SST anomalies in the present model is associated with the first EOF which has amplitudes confined to the central-eastern Pacific (Fig. 2a), the timeseries of $A_1$ alone closely represents a warm or cold event and its evolution. The second reason, which is more relevant for the present purpose, is that the $A_k$ represent active links between the ocean and atmosphere in our approach. They are not only the projections of SST anomalies onto the EOFs, but also the strength of the corresponding wind anomalies. Cold SST anomalies in the central Pacific imply negative $A_1$, for example, which implies an easterly wind anomaly in the central-western Pacific and hence an accumulation of water in the west Pacific, which normally has negative feedbacks on $A_1$ through the ocean dynamics and thermodynamics.

Fig. 6a shows the time evolution of $A_1$ for the 1982/83 event, for the control (solid line) and five predictions (column 3 of Table 1). This event was dominated by the first EOF. Corresponding timeseries of $A_2$ and $A_3$ have smaller amplitude variations with shorter timescales. The predictions closely followed the general trend of the control run in the first EOF, but not in the higher modes, implying that the accuracy of the model prediction depends strongly on the first EOF.

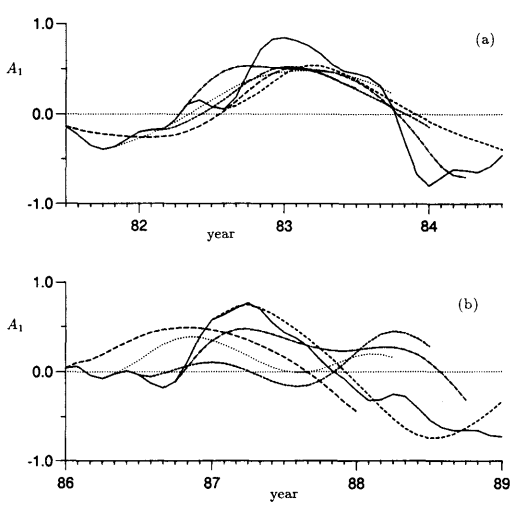


*Fig. 6.* Timeseries of coefficients $A_1$ for the first EOF of SST anomalies, for the control run (solid) and 5 predictions (broken lines), for (a) the 1982/83 warm event, and (b) the 1986/87 warm event.

Corresponding plots for five predictions of the 1986/87 event (column 4 of Table 1) are shown in Fig. 6b. In this case, the predicted $A_k$ did not follow the control run very well, except for the experiment starting in January 1987 which did trace the temporal evolution of the first EOF. Comparing with Fig. 6a, it is noted that the predictions of the 1986/87 event were started with very small $A_1$ (except for the January 1987 start), which would be associated with very weak wind anomalies. In other words, at the starting points, the system was in a state of weak wind and temperature anomalies; it had to evolve further to let the anomalies grow toward positive or negative phase, constrained by the mechanism of natural oscillation in the model. In fact, the coefficients $A_2$ of the second EOF at the starting points of April, July and October 1986 had comparable amplitudes to $A_1$; the growing phases were presumably determined by the combination of the two EOFs.

By contrast, predictions for the 1982/83 event were started during or just after a period with considerable amplitude of the dominant $A_1$, indicating that the system had experienced preconditioning. (Note that, according to the structure of the ENSO mode in Fig. 3 revealed by POP analysis, large amplitude of $A_1$ is usually associated with large heat content anomalies in the west Pacific.) For the 1982/83 event, easterly wind anomalies associated with negative $A_1$, for example before January 1982, had piled up positive layer depth anomalies in the western Pacific, which, after reflection from the western boundary, tend to switch off the negative phase of $A_1$ according to the delayed oscillator scenario. In this theory, the time needed to switch $A_1$ from one phase to another is related to the amount of accumulated water which is roughly proportional to the strength of the wind anomalies and hence of $A_1$ at the start. This may explain why it took longer to switch $A_1$ from negative to positive for the July 1981 prediction

than for the October 1981 prediction, since the magnitude of $A_1$ in the former was smaller than in the latter.

The amplitude of $A_1$ may therefore contain important preconditioning information. When it is small for several months, higher EOF modes may play comparable roles to that of the first EOF; the system is then not well preconditioned since there is no significant accumulation of water in the equatorial west Pacific, but the small anomalies are going to develop in the freely coupled mode because of coupled instabilities. Substantial amplitude of $A_1$, on the other hand, indicates that the system has experienced preconditioning by accumulating warm or cold water in the west Pacific, which normally has negative feedback effects on $A_1$, i.e., the system is able to change phase when released from the forced run. It appears that the 1986/87 event was not well preconditioned in the model, as $A_1$ remained near zero during much of 1986.

The dependence of the model prediction behavior on the initial amplitude of the first EOF projection $A_1$ was examined by calculating the prediction errors as a function of the initial value of $A_1$ (denoted $A_{1t_0}$) and of lead time for all 100 predictions. The prediction error is defined as the difference between the Niño3 SST anomalies of the prediction and the control run. This error grows as the lead time increases for lead times up to about 5 months, with little dependence on $A_{1t_0}$ at first. For lead times from about 3 to 7 months, the errors tend to be smaller for larger amplitude of $A_{1t_0}$ (positive or negative) than for smaller $A_{1t_0}$: Fig. 7 shows how individual errors depend on $A_{1t_0}$ at a lead time of 6 months. This is consistent with the case studies of the 1982/83 and 1986/87 events. In other words, for initial conditions with considerable amplitude of $A_{1t_0}$, the model is more likely to be able to catch the evolution of the control run. At longer lead times there is no clear relation between the errors and $A_{1t_0}$. The memory inherent in the ocean model suggests that it may also be useful to investigate lag correlations of errors and $A_k$.

### 4.2. *Ensemble features*

In the case studies in Subsection 4.1, we have shown that the model can do a good job of predicting SST anomalies for ENSO events. In a quiet period of weak anomalies in the wind and SST, however, predictions using this model are less reliable. This is probably a common feature for all the existing coupled models used for ENSO prediction. In this subsection, the ensemble features of all 100 prediction experiments are presented, in order to get an overall estimate of the skill of the model prediction, including both ENSO events and quiet periods.

To measure the prediction skill, correlations of predicted Niño3 SST anomalies with corresponding anomalies for both the control run and observations were calculated as a function of lead time, together with the corresponding root mean square (rms) errors. The rms error is normalized by the standard deviation of the predictand, i.e., SST anomalies of the control run or observations. Fig. 8 shows the correlations and rms errors for the Niño3 region, for predictions compared to the control run (curves labelled C), averaged over 100 datasets. In contrast to Fig. 5 for the selected ENSO cases, it is seen that the correlation for the full dataset is above 0.5 only up to a lead time of about 7 months. The correlation calculated for the full dataset has large detrimental contributions from the quiet periods of weak anomalies, which the model could not predict very well. The rms errors show a sharp growth for lead times up to about 9 months, after which the errors tend to

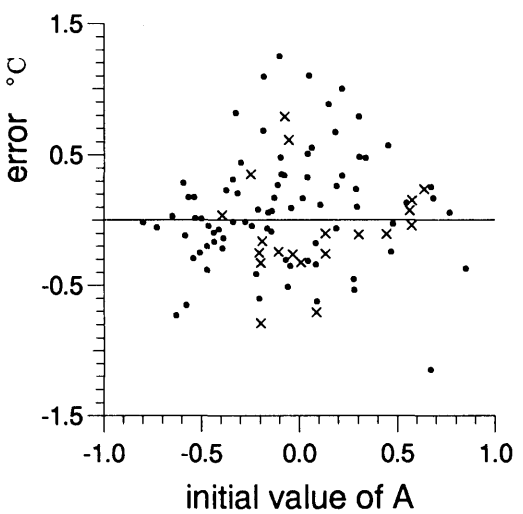


*Fig. 7.* Prediction errors (prediction minus control) for Niño3 SST anomalies as a function of the initial value $A_{1t_0}$ for 100 experiments, for a lead time of 6 months. The 20 special ENSO cases (Table 1) are marked by ×.



Tellus A/46/4-10

saturate. By a lead time of 7 months, the rms errors have reached the level of the standard deviation of the control run, which may be considered as an upper limit for useful prediction as far as the amplitude is concerned.

For comparison, correlations and rms errors between the predicted and the observed SST anomalies in the Niño3 region are also shown in Fig. 8 (curves O). The model errors relative to the observations in the forced simulation are indicated by the correlation at zero lead time, which is about 0.75. Starting from this value, the drop in the correlation as a function of lead time is more gradual than that for the comparison against the control run, but again dropping below 0.5 at a lead of 7 months. The rms errors show a rather linear increase as a function of the lead times shown, and the error reaches the standard deviation at a lead time of about 12 months for the full dataset.

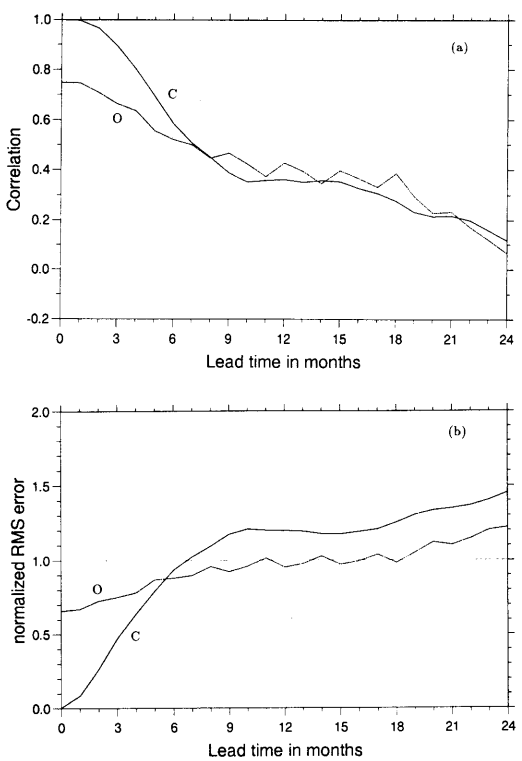


*Fig. 8.* Correlations and rms errors between predictions and values of SST anomalies in the Niño3 region as a function of lead time. Curves labelled C are for comparisons with SST from the control run, while label O indicates comparisons with SST from observations. (a) correlations, (b) rms errors, normalised by the standard deviation of observations (curve O) or control values (curve C).

The seasonal dependence has also been examined: there are variations between the seasons, but they are not nearly as large as the variations reported for models with explicit seasonal dependence in the mean state (e.g., Latif et al., 1994; Balmaseda et al., 1994), which suggests that the seasonal dependence of the prediction skill results mainly from the seasonally-varying basic state.

## 5. Comparison with a POP prediction scheme

A prediction scheme based on POP modes like that proposed by Xu and Von Storch (1991) is considered. The prediction method, based on a single ENSO-related POP mode, is to first specify an initial location for the mode in the real versus imaginary amplitude space according to the control run, and then to follow the free trajectory in that space. The trajectory is unable to provide useful information about the future amplitude of the evolution as the trajectory will spiral toward the origin in the absence of some forcing. Nevertheless, one can concentrate on the phase determined by the mode, under the assumption that the desired exciting forcing is always present in the system to keep the mode energetic. The problem is thus reduced to identifying the location of a given initial state on the POP cycle. The ENSO-related POP mode used for the following predictions was that described in Section 3, obtained by analyzing the combined dataset of model SST, layer depth and zonal wind stress anomalies from the control run.

The dial plots in Fig. 9a–e show the evolution of the control run (solid lines) and POP predictions (broken lines) for the 5 selected ENSO cases (Table 1), with amplitudes of the real and imaginary POP patterns as axes. In general the evolutions show a clockwise rotation around the origin for the control run; the peak phase can be estimated as being when a trajectory crosses negative (positive) maximum imaginary values for a warm (cold) event (see the spatial patterns in Fig. 3). The predictions start at initial conditions 3 months apart, as for the dynamical model, but the decay factor of the amplitude has been excluded in the diagram for reasons mentioned above. The

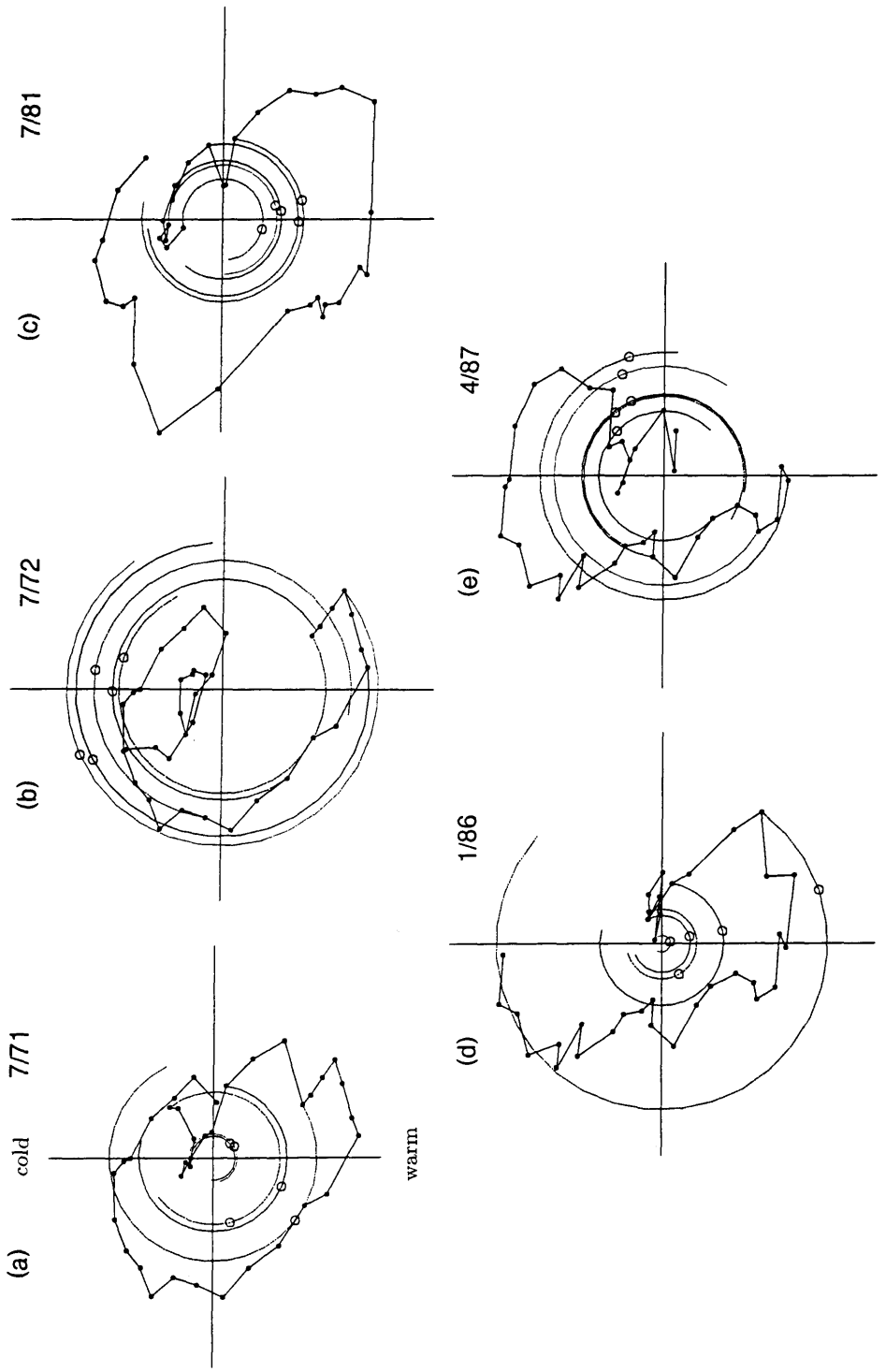


*Fig. 9.* Dial plots of the coefficients of real (horizontal axis) and imaginary (vertical axis) spatial patterns for the ENSO-related POP mode, for 5 ENSO cases. The solid curves are values from the control run, with dots at monthly intervals. Broken lines show predicted trajectories (see Table 1 for start dates). The number at the top-right of each diagram is the starting time of the first prediction: others following at three month intervals. Open circles mark the time of peak phase of the control run, which is warm for (a), (c), (d); cold for (b) and (e).

open circles on the prediction lines mark the time when the peak phase was reached in the control run, so a good prediction would have the circles located close to the negative (warm event) or positive (cold event) imaginary axis. It is seen that many of the predictions match the control run fairly well, except for the case of the 1988/89 cold event (Fig. 9e) in which all the predictions reached the peak phase about 6 months earlier than the control run. For the 1972/73 warm event (Fig. 9a), the prediction starting in July 1971 reached the peak phase about 4 months earlier than the control run, as also observed in the dynamical model prediction. The 1982/83 warm event shows up again as a successful prediction; all the circles are located close to the negative imaginary axis. It is of interest to note that in the case of POP prediction, 3 out of the 5 predictions for the 1986/87 warm event (Fig. 9d) are in fair agreement with the control run phase, in contrast to the dynamical model predictions which were unsuccessful.

The 1986/87 warm event illustrates the difference between the two schemes: the POP scheme did a better job than the dynamical model for predictions starting in April, July and October 1986. The difference arises because the two schemes concentrate on different elements of the ENSO mechanism. Both schemes are able to identify the amplitude and location of an initial state in the cycle of the natural oscillation of the model. While the dynamical scheme traces the evolution by the amplitude and phase, the POP scheme captures only the cyclic character, leaving the amplitude undetermined. In other words, the POP prediction scheme picks up only the phase configuration of the patterns (Fig. 3) at the start, and the evolution afterwards is independent of the amplitude of the initial configuration. However, using the same configuration as the initial condition, the evolution of the dynamical prediction scheme (which is amplitude dependent) could be growth or decay, and the oscillation character could also depend on the amplitude.

## 6. Discussion and summary

In order to gain better understanding of the predictability of ENSO in coupled ocean-atmosphere models, we have focused on model predictions in a simple coupled system. The ocean component used consists of a one-and-half layer, reduced gravity model with a prognostic equation for SST. The empirical atmosphere is constructed by using a statistical technique to relate the observed wind anomalies to the model-simulated SST anomalies. The results show that the empirical atmosphere could capture the basic atmospheric response to SST anomalies, particularly on ENSO time scales. A point of interest was to examine how the model catches or misses a target event.

The case studies show that the ability of the model to predict an event was best when it could identify preconditioned information in the initial conditions. It seemed more difficult for the model to follow a quiet evolution of weak anomalies in the wind and SST. This behavior can be explained by the mechanism responsible for the interannual variations in the model. When the prediction is started, the system is released from the forced mode to a free evolution determined by the natural oscillation mechanism of the model. At the start of a prediction, it is necessary for the model to identify where the given initial condition is on the trajectories of its own natural oscillation cycle. For initial conditions with well preconditioned information, i.e., current or recent large amplitude of $A_{1_{t_0}}$ in our model, the trajectory of the prediction is more likely to match that of the evolution observed in the control run, since the system in the coupled mode could pick up essentially the same mechanism that is responsible for the variations on this time scale. A mismatch of the trajectories of the prediction and control, on the other hand, indicates that the evolution of the control may not be due to the same mechanism as that which the prediction model has picked up. This is probably true in the present model, as the mismatches were observed mostly during quiet periods in which the variations had small amplitudes and shorter time scales that were likely caused by effects other than the ENSO mechanism.

A comparison was made between the dynamical model prediction and a POP prediction scheme. It was shown that the prediction skills of both schemes come from their ability to capture, at least partly, the mechanism of the ENSO cycle. While the dynamical model could identify both amplitude and phase of an initial condition in the natural oscillation cycle, the POP scheme only needed the phase information from the initial condition and gave no amplitude estimation for the

future evolution. Both schemes showed, in general, comparable skills for prediction of the events, although differences were observed for individual predictions. It should be pointed out that the POP analysis was carried out by using the combined dataset; so the POP scheme contains information not only of SST, but also of heat content anomalies. It would be of interest to examine the prediction skill of the dynamically coupled model when heat content information is included in the prediction scheme, as in Balmaseda et al. (1994).

Another important effect on the predictive skill is the inevitable errors in the initial conditions, which could be responsible for the quick drop in the correlations during the first few months of lead time (Fig. 8). Goswami and Shukla (1992) and Blumenthal (1991) have discussed this issue from different approaches. We have instead concentrated on the long term behaviour of the predictions in this study. A thorough investigation of the model prediction skill of ENSO, however, should include both the short term (first few months) and long term behaviour.

## 7. Acknowledgements

The authors wish to thank M. R. Allen and M. A. Balmaseda for their substantial assistance with the statistical techniques used in the study. This work was partly supported by the NERC through grant GR3-7366.

## 8. Appendix. An application of principal oscillation pattern analysis

Suppose that we have information about $M$ spatial components of a system $Z$ at $N$ timepoints at intervals $\Delta t$, represented in terms of EOFs and timeseries of their coefficients. A subset containing $L$ of those functions (chosen such that most of the variance of the original system is retained) is used to partially reconstruct the system as

$$\underline{\underline{Z}} = \underline{\underline{E}}\,\underline{\underline{A}}^{\mathrm{T}} \tag{A1}$$

where each column of $\underline{\underline{E}}$ is an EOF spatial pattern and each row of $\underline{\underline{A}}$ is a timeseries. Thus,

$$Z(x_m, t_n) = \sum_{l=1}^{L} E_l(x_m)\, A_l(t_n)$$

(cf. eq. (2)). We want to represent the temporal evolution by a first-order Markov process:

$$A_l(t_{n+1}) = \sum_{k=1}^{L} \alpha_{lk} A_k(t_n) + \text{noise}. \tag{A2}$$

Put

$$\hat{A}_l(t_{n+1}) = \sum_{k=1}^{L} \alpha_{lk} A_k(t_n). \tag{A3}$$

Then minimising $\sum_l \sum_n (\hat{A} - A)^2$ requires:

$$\underline{\underline{\alpha}} = \underline{\underline{C}}^{(1)} \underline{\underline{C}}^{(0)^{-1}} \tag{A3}$$

where

$$C^{(i)}_{pq} = \sum_n A_p(t_{n+i})\, A_q(t_n)$$

is a lag-$i$ covariance. Independent modes of the first-order process can be determined from the eigenvalues $\eta$ and eigenvectors $\boldsymbol{e}$ of $\underline{\underline{\alpha}}$, which (as $\underline{\underline{\alpha}}$ is real) are real or occur in complex conjugate pairs. Suppose $\eta = \rho e^{i\omega}$, and $\boldsymbol{e} = \boldsymbol{e}_{\mathrm{R}} + i\boldsymbol{e}_{\mathrm{I}}$, for an oscillating mode with period $\tau = (2\pi/|\omega|)\,\Delta t$ and decay time $D = -\Delta t/\ln \rho$. The system $Z$ can be rewritten in terms of these modes. It is convenient to define a real matrix $\underline{\underline{B}}$ by taking as its columns pairs $\boldsymbol{e}_{\mathrm{R}}$ and $\boldsymbol{e}_{\mathrm{I}}$ from one of each complex conjugate pair, together with the real $\boldsymbol{e}$s that correspond to non-oscillatory modes. There are $L$ such vectors, and they usually form a complete set. Define new timeseries of coefficients $P$ for the independent modes by

$$\underline{\underline{P}} = \underline{\underline{A}}(\underline{\underline{B}}^{-1})^{\mathrm{T}}. \tag{A4}$$

Then (A2) becomes

$$P_l(t_{n+1}) = \sum_{k=1}^{L} (\underline{\underline{B}}^{-1}\underline{\underline{\alpha}}\,\underline{\underline{B}})_{lk}\, P_k(t_n) + \text{noise}. \tag{A5}$$

The matrix $\underline{\underline{B}}^{-1}\underline{\underline{\alpha}}\,\underline{\underline{B}}$ contains $2 \times 2$ rotation matrices along its diagonal for the oscillating modes. Rows of $\underline{\underline{P}}$ are POP timeseries, containing coefficients for independently evolving noise-forced modes. Pairs of timeseries are denoted $P_{\mathrm{R}_j}(t_n)$ and $P_{\mathrm{I}_j}(t_n)$ for the "real" and "imaginary" parts of the $j$th oscillatory mode.

From (A1), the original system can be expressed as

$$\underline{\underline{Z}} = \underline{\underline{E}}\,\underline{\underline{B}}\,\underline{\underline{P}}^{\mathrm{T}} = \underline{\underline{POP}}\,\underline{\underline{P}}^{\mathrm{T}}. \tag{A6}$$

The columns of the matrix $\underline{\underline{POP}} = \underline{\underline{E}}\underline{\underline{B}}$ are spatial patterns formed by linear combinations of EOFs. Pairs of patterns are denoted $pop_{R_j}$, $pop_{I_j}$ for the $j$th oscillatory mode. Note that the system at any time can be projected onto the POP modes by using spatial patterns $\underline{\underline{PROJ}} = \underline{\underline{E}}(\underline{\underline{B}}^{-1})^{T}$.

Although the oscillation and decay timescales are well defined in the above outline, the spatial patterns and corresponding timeseries can be altered by manipulating $\underline{\underline{B}}$. In this paper we remove this ambiguity by scaling the eigenvectors $\boldsymbol{e}$ such that $\boldsymbol{e} \cdot \boldsymbol{e} = 1$ and $\boldsymbol{e}_R \cdot \boldsymbol{e}_I = 0$. One consequence of this choice is that the pairs of spatial patterns $pop_R$, $pop_I$ have the same orthonormal property.

Suppose $\underline{\underline{Z}}$ is partially reconstructed using, for example, the $j$th oscillating POP mode:

$$Z_j^{\text{part}}(x_m, t_n) = pop_{R_j}(x_m)\, P_{R_j}(t_n) + pop_{I_j}(x_m)\, P_{I_j}(t_n). \tag{A7}$$

Denote the variance of $\underline{\underline{Z}}_j^{\text{part}}$ by $V_j^{\text{part}}$. The partial variances of the oscillating and purely decaying modes cannot simply be added to obtain $Var(\underline{\underline{Z}})$. We define fractional partial variance, as used in Section 3, by

$$F_j = V_j^{\text{part}} \Big/ \sum_{\text{all modes}} V^{\text{part}}. \tag{A8}$$

## REFERENCES


Balmaseda, M. A., Anderson, D. L. T. and Davey, M. K. 1994. ENSO prediction using an intermediate ocean model coupled to statistical atmospheres. *Tellus* **46A**, 497–511.

Barnett, T. P., Latif, M., Graham, N., Flügel, M., Pazan, S. and White, W. 1993. ENSO and ENSO related predictability, Part 1: Prediction of equatorial sea surface temperature with a hybrid coupled ocean-atmosphere model. *J. Clim.* **6**, 1545–1566.

Blumenthal, M. B. 1991. Predictability of a coupled ocean-atmosphere model. *J. Clim.* **4**, 766–784.

Cane, M. A., Zebiak, S. E. and Dolan, S. C. 1986. Experimental forecasts of El Niño. *Nature* **321**, 827–832.

Davey, M. K., Ineson, S. and Balmaseda, M. A. 1994. Simulation and hindcasts of tropical Pacific Ocean interannual variability. *Tellus* **46A**, 433–447.

Gill, A. E. 1980. Some simple solutions for heat-induced tropical circulation. *Q. J. Roy. Met. Soc.* **106**, 447–462.

Goldenberg, S. D. and O'Brien, J. J. 1981. Time and space variability of tropical Pacific wind stress. *Mon. Weath. Rev.* **109**, 1190–1207.

Goswami, N. E. and Shukla, J. 1991. Predictability of a coupled ocean-atmosphere model. *J. Clim.* **4**, 3–22.

Hasselmann, K. 1988. PIPs and POPs: the reduction of complex dynamical systems using Principal Interaction and Oscillation Patterns. *J. Geophys. Res.* **93**(D9), 11015–11021.

Latif, M. and Flügel, M. 1991. An investigation of short range climate predictability in the tropical Pacific. *J. Geophys. Res.* **96**(C2), 2661–2673.

Latif, M., Sterl, A., Maier-Reimer, E. and Junge, M. M. 1993. Climate variability in a coupled GCM. Part 1: the tropical Pacific. *J. Clim.* **6**, 5–21.

Latif, M., Barnett, T. P., Cane, M. A., Flügel, M., Graham, N. E., Von Storch, H., Xu, J.-S. and Zebiak, S. E. 1994. A review on ENSO prediction studies. *Climate Dyn.* **9**, 167–179.

Latif, M., Barnett, T. P. and Mizuno, K. 1992. *Model structure of variations in the tropical climate system.* Part 1: *Observations*. Max-Planck-Institut für Meteorologie, report no. 91.

McCreary, J. P. and Anderson, D. L. T. 1991. An overview of coupled ocean-atmosphere models of El Niño and the Southern Oscillation. *J. Geophys. Res.* **96**, 3125–3150.

Neelin, D., Latif, M. and Jin, F.-F. 1994. Dynamics of coupled ocean-atmosphere models. *Ann. Rev. Fluid Mech.* **26**, to appear.

Rasmusson, E. M. and Carpenter, T. H. 1982. Variations in tropical sea surface temperature and surface wind fields associated with the Southern Oscillation/El Niño. *Mon. Weath. Rev.* **110**, 354–384.

Von Storch, H., Bürger, G., Schnur, R. and Von Storch, J.-S. 1993. Review paper: *Principal Oscillation Patterns*. Max-Planck-Institut für Meteorologie report no. 113.

Wu, D.-H., Anderson, D. L. T. and Davey, M. K. 1993a. ENSO variability and external impacts. *J. Clim.* **6**, 1703–1717.

Wu, D.-H., Anderson, D. L. T. and Davey, M. K. 1993b. *ENSO prediction experiments using a simple ocean-atmosphere model.* UKMO Climate Res. Tech. note no. 39.

Xu, J.-S. and Von Storch, H. 1990. Principal oscillation patterns-prediction of the state of ENSO. *J. Clim.* **3**, 1316–1329.